Supporting Information for A Universal Length-Dependent Vibrational Mode in Graphene Nanoribbons

Jan Overbeck,[*,†,‡,¶,@] Gabriela Borin Barin,[†,@] Colin Daniels,[§,@] Mickael L. Perrin,[†] Oliver Braun,[†,‡] Qiang Sun,[†] Rimah Darawish,[†,‖] Marta De Luca,[‡] Xiao-Ye Wang,[⊥,△] Tim Dumslaff,[⊥] Akimitsu Narita,[⊥] Klaus Müllen,[⊥,#] Pascal Ruffieux,[†] Vincent Meunier,[*,§] Roman Fasel,[*,†,‖] and Michel Calame[*,†,‡,¶]

†*Empa, Swiss Federal Laboratories for Materials Science and Technology, 8600 Dübendorf, Switzerland*

‡*University of Basel, Department of Physics, 4056 Basel, Switzerland*

¶*University of Basel, Swiss Nanoscience Institute, 4056 Basel, Switzerland*

§*Rensselaer Polytechnic Institute, Department of Physics, Applied Physics, and Astronomy, Troy, New York 12180, United States*

‖*University of Bern, Department of Chemistry and Biochemistry, 3012 Bern, Switzerland*

⊥*Max Planck Institute for Polymer Research, 55128 Mainz, Germany*

#*Institute of Physical Chemistry, Johannes Gutenberg-Universität Mainz, 55128 Mainz, Germany*

@*These authors contributed equally.*

△*Current address: State Key Laboratory of Elemento-Organic Chemistry, College of Chemistry, Nankai University, Tianjin 300071, China*

E-mail: jan.overbeck@empa.ch; meuniv@rpi.edu; roman.fasel@empa.ch; michel.calame@empa.ch

Contents:

SI Note 1 - Sample fabrication and STM data

Throughout this study, the following types of samples were used: Aligned ribbons grown on vicinal Au crystals - Au(788) or Au(11,12,12). Spectra of AGNRs acquired directly on these Au crystals are referred to as "on Au(788)". These samples were transferred onto a target substrate using an electrochemical delamination process with a PMMA support layer, referred to as "bubbling transfer".[1] Mostly, these substrates are Raman-optimized (RO) device type substrates.[2] Spectra acquired after "bubbling transfer" are labeled "on substrate/BT". The second type of sample is prepared on thin (200 nm) gold films supported on Mica (*PHASIS, Geneva, Switzerland*), which exhibit much wider Au(111) terraces (see Figure S3 b) for an STM image). These samples are referred to as "on Au/Mica". They are transferred onto substrates in a polymer-free transfer by cleaving off the mica and etching away the Au-layer.[3] Spectra acquired after the "polymer-free transfer" method are labeled "on substrate/PFT". Finally, AGNRs of the same width can be produced from different precursor molecules, specifically, precursors with reactive groups based on bromine or, alternatively, iodine. These details are listed in Table S1 below.

Table S1: Details for samples used throughout this study.

Sample label	Precursor-halogen	Substrate	Transfer method	Figures
5-1_Au	Iodine	Au(788)	-	1 a, b), 3 c), S1 b)
5-2_Au	Iodine	Au/Mica	-	2 c), S3 a), S8 a)
5-3_Au	Iodine	Au(788)	-	2 c), S3 a)
5-4_Au	Iodine	Au/Mica	-	2 c)
5-5_Au	Iodine	Au/Mica	-	2 c), S3 a)
5-6_Au	Bromine	Au(788)	-	2 b), S3 a), S8 b)
5-6_T	Bromine	RO	BT	S8 b)
5-7_T	Iodine	Si/SiO_2	BT	S8 a)
5-8_Au	Bromine	Au(788)	-	S2, S3 a), S11
5-8_T	Bromine	RO	BT	S11 b), S14 b)
5-9_Au	Iodine	Au/Mica	-	S3 a, b)
5-10_Au	Bromine	Au/Mica	-	S3 a)
7-1_T	Bromine	RO	PFT	1 b), S6
7-2_T	Bromine	RO	BT	S10 a)
9-1_T	Iodine	RO	BT	1 b), S13 b)
9-2_T	Iodine	RO	PFT	4 a), S12
9-3_Au	Iodine	Au(788)	-	S9 a)
9-4_T	Iodine	Au(11,12,12)	-	S9 b), S10 b)

STM images of GNRs on growth substrates

STM imaging is the prime technique for investigating GNRs on their growth substrate in UHV, occasionally complemented with non-contact atomic force microscopy.[4] Here we focus on two types of STM, room-temperature STM (RT-STM or just STM) and low-temperature STM (LT-STM). Figure S1 a) below shows STM images of a bare Au(788) vicinal crystal, showing the precisely aligned terraces. Figure S1 b) displays a Au(788) crystal after growth of 5-AGNRs. The GNRs grow predominantly along the direction of the terraces (see insets). In contrast to 7- and 9-AGNRs, significant step bunching is observed for 5-AGNRs, resulting in wider terraces compared to the bare substrate. Here, the 5-AGNRs are visible for imaging at room temperature, because the sample contains predominantly long GNRs, which are relatively immobile. The Raman spectrum in Figure 1 of the main manuscript was acquired on this exact sample (5-1_Au).

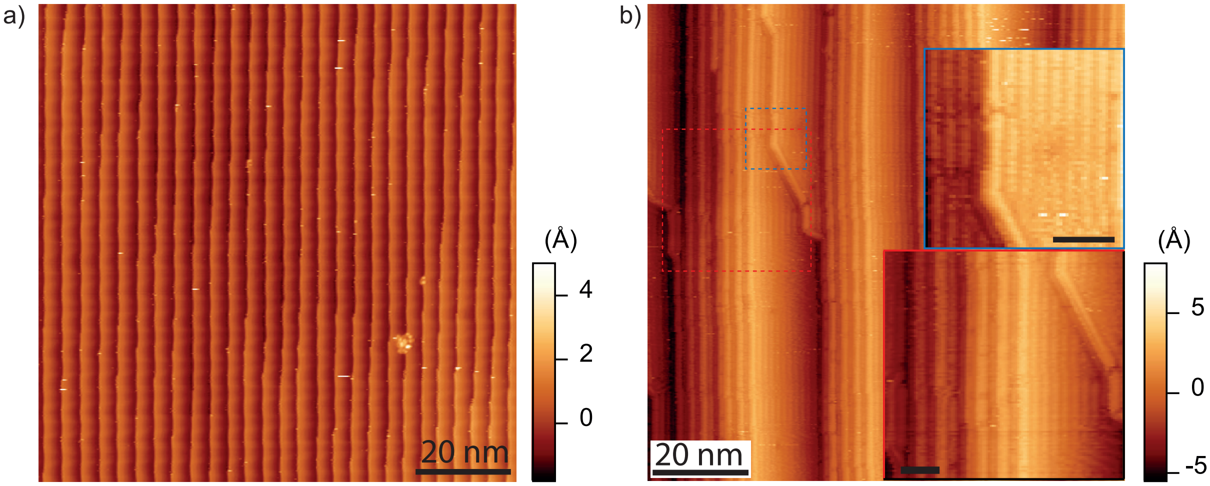

Figure S1: Room-temperature STM of a Au(788) growth substrate before and after growth of long 5-AGNRs. a) Bare Au(111) terraces on a Au(788) single crystal substrate. **b)** Long, aligned 5-AGNRs grown on Au(788) with significant step-bunching. Insets: zoom onto the terrace-regions indicated by dotted squares, revealing parallel GNRs. Scale bar: 5 nm. Sample 5-1_Au

LT-STM on short 5-AGNRs

Samples containing short ribbons are difficult to image at room temperatures, because smaller GNRs are dragged along the surface by the scanning probe, resulting in fuzzy areas on the image. For these samples, high-resolution LT-STM (T=5 K) images were recorded to visualize these short 5-AGNRs. Figure S2 shows two images of a sample that contains a large number of very short GNRs. The corresponding Raman spectrum is shown in Figure S3 a), labeled 5.Br.06. The inset of Figure S2 b) clearly shows an assembly of very short (2-5 nm) GNRs. Note, that the short ribbons on the larger terraces are nearly randomly oriented, while they are aligned with the crystal direction on the narrower terraces. An image processing script was used to extract the length of GNRs in well-resolved areas. The corresponding histogram for this sample is shown as an inset, confirming a majority of very short GNRs. Specifically, the GNRs with a length below 2/3/4 nm correspond to 4/6/8-unit 5-AGNRs (see Figure S5 for corresponding structures).

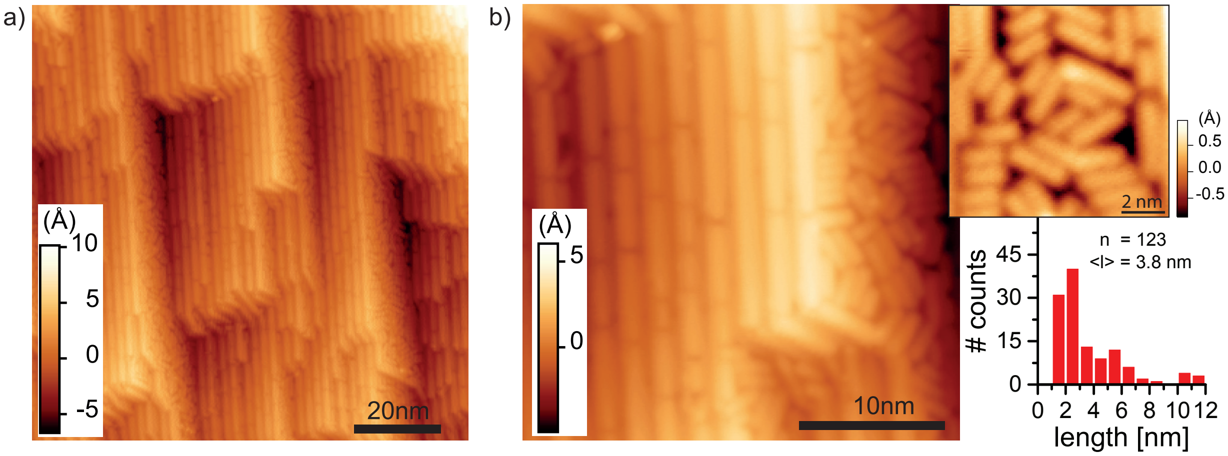

Figure S2: Low temperature STM images of short, aligned 5-AGNRs. a) Overview scan of a sample produced from partially debrominated precursor molecules resulting in short 5-AGNRs on a Au(788) crystal with pronounced step-bunching. **b)** High resolution scan from a) clearly revealing a large amount (∼ 50%, see histogram) of 4-, 6-& 8-unit 5-AGNRs. Sample 5-8_Au.

Correlation of Raman spectra with STM images.

For the case of 5-AGNRs, in total, we investigated 15 samples (9 shown here) directly on the growth substrates, Au(788) and Au/Mica. Of these, 12 (3) were grown from iodine(bromine)-based precursors, respectively. A study about the optimization of GNR growth parameters will be published elsewhere. The STM characterization of most samples was carried out at room temperature. Therefore, the amount of short GNRs is inferred from the prevalence of fuzzy areas/ areas not showing long, well-aligned AGNRs. In Figure S3 a) we plot Raman spectra of 7 representative samples. All samples, except those with optimized growth recipes, show the LCM attributed to 4-/6-/8-unit long 5-AGNRs. The STM image of an optimized sample grown on Au/Mica is shown in Figure S3 b), along with a histogram of ribbon length. Note, that very long GNRs extending beyond the scan range were not counted into the

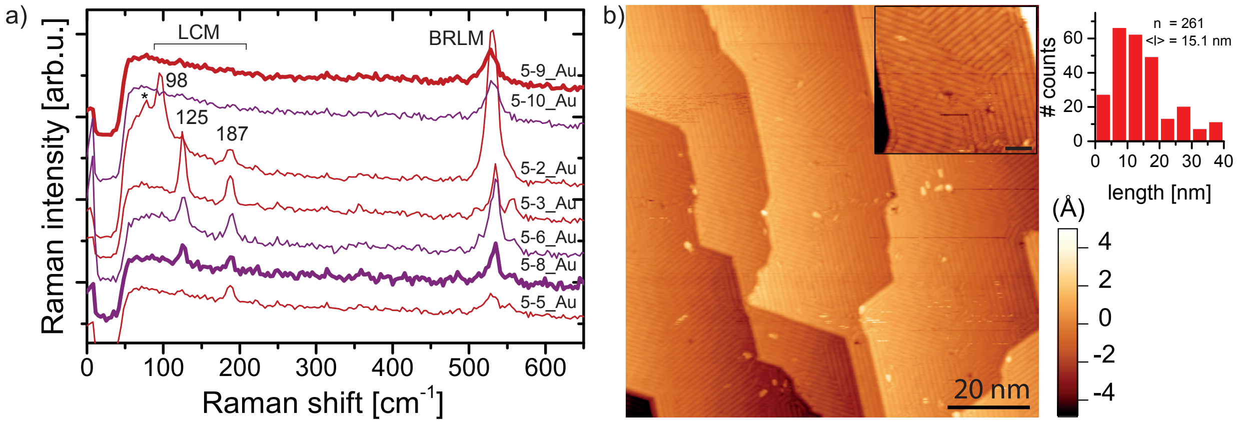

Figure S3: Sample comparison of 5-AGNRs on gold with different LCM-contributions for both precursor halogens. a) Raman spectra for 5-AGNR samples with different length distributions. Samples synthesized from both Br/I-based precursors (purple/red) are shown to produce both long and short GNRs. Spectra shown with bold lines correspond to STM images in panel b) (Sample 5-9_Au) and Figure S2 (Sample 5-8_Au). **b)** STM image of Sample 5-9_Au containing predominantly long 5-AGNRs. Scale bar of inset 5 nm. Histogram shows the length distribution extracted from the STM image.

histogram at all which likely leads to an underestimated average GNR length. Nevertheless, with an optimized growth recipe one achieves lengths comparable to that of previously optimized 7- and 9-AGNR growth recipes.[3,5]

For the samples with a significant amount of short ribbons we identify the characteristic LCM peak positions at Raman shifts of approximately 98 cm^{-1}, 125 cm^{-1} and 186 cm^{-1} as well as the RBLM at about 530 cm^{-1}. The spectra are arranged according to the presence of the LCM, with increasing contribution of LCM-98/125/186 from top to bottom. We do not observe any change in frequency of these peaks when changing between bromine- and iodine-based precursors. The trend observed here agrees well with the observations from RT-STM. A quantitative analysis is hampered by the prohibitive time consumption for low-temperature STM analysis on each sample, highlighting the benefit of rapid identification of short GNRs by Raman spectroscopy.

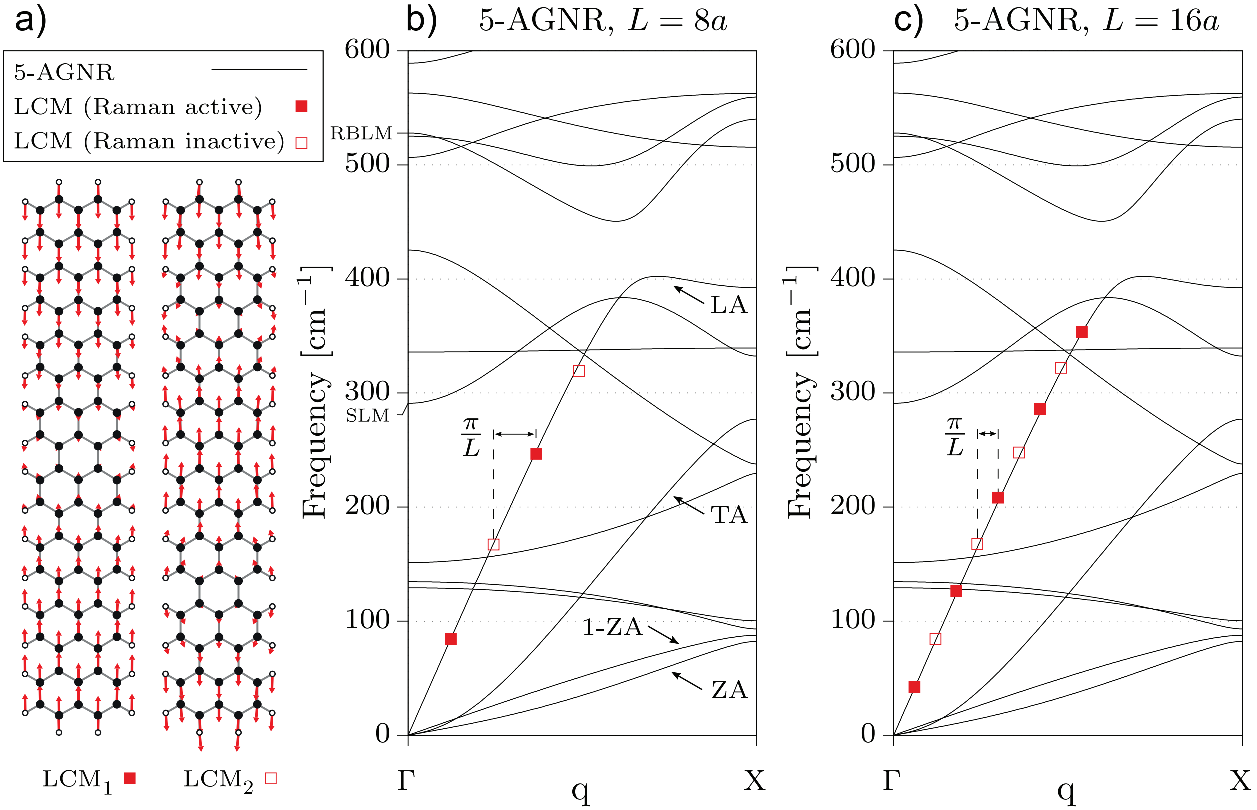

Figure S4: Origins of the LCM modes in 5-AGNRs. a) Longitudinal Compressive Mode (LCM_1) and its first overtone (LCM_2) for a finite-size 5-AGNR of length $L = 8a$. **b)** The phonon dispersion relations of a periodic 5-AGNR is plotted with black curves and is characterized by four acoustic branches marked by symbols LA, TA, ZA, and 1-ZA[6]. The calculated frequencies of longitudinal compressive modes are represented at constant interval $\pi/(Na)$ for $N = 8$. Similar results are shown for $N = 16$ in **c)**. In both cases, Raman active and inactive modes are shown with full and hollow squares, respectively. For reference, note that the shear-like mode (SLM) and the radial-breathing mode (RBLM) are located at $290\,\mathrm{cm}^{-1}$ and $527\,\mathrm{cm}^{-1}$. Additional length-dependent modes (not shown) emerge from the zone-folding procedure applied of the TA, ZA, and 1-ZA branches with the appearance of in-plane bending, twisting, and out-of-plane bending modes, respectively.

SI Note 2 - Fundamental origin of the LCM

We will first discuss the fundamental origin of the LCM and its overtones in finite-size nanoribbons. We will show that the emergence of these modes stems directly from a zone-folding effect that accounts for the dimensionality reduction of a 1D periodic GNR into a 0D finite-size GNR. In a 1D GNR, the quasi-momentum q spans continuous values from 0 to π/a of the 1D Brillouin zone, where a is the GNR's lattice vector. Ignoring the effects of end-passivation, creating a finite size GNR of length L is thus expected to lead to the selection of allowed values of the 1D momentum as a set of discrete values:

$$q_i = i\frac{\pi}{L} \tag{1}$$

where $L = Na$, N is the number of unit cells along the GNR's axis, and $i = 0, \ldots N - 1$.

1D nanostructures are characterized by the presence of 4 acoustic branches (see, Figure S4 a)).[6] Three branches correspond to three acoustic modes (LA, TA, and ZA) in the longitudinal, transverse, and perpendicular directions of graphene. The fourth acoustic mode is a typical mode found in 1D nanostructures: it corresponds to a rotation around the periodic axis of the structure. The LCM mode and its overtones arise from the quantization of q along the LA branch.

The mapping of the phonon bandstructure from a 1D to a finite-size ribbon is equivalent to selecting modes that are separated by $i\pi/Na$ along the Brillouin zone. This effect is illustrated for two 5-AGNRs of size $N = 8$ and $N = 16$ in Fig. S4, using the REBOII potential. In this figure, we plot the values of the low-frequency modes calculated explicitly on finite-size ribbons and place them on the dispersion relation of a 1D 5-AGNR at regular π/L intervals. Note that the Brillouin zone for the finite length structures is reduced to a single point and thus exciting those modes corresponds to a zero net momentum transfer. It follows that when Raman active, these modes can potentially be involved in 1st-order Raman processes. The data points all fall closely on the linear branch associated with GNR's LA mode, showing that the ending hydrogen atoms do not have a significant effect on this mode. As expected for an LA branch and as shown in Figure S4 a) for the fundamental vibration and its first overtone, these modes correspond to longitudinal compressive modes. Interestingly, only modes with odd values of i ($\mathrm{A_g}$ symmetry vs. $\mathrm{B_{1u}}$ symmetry for even values of i) are Raman active, since only they are associated with a net change of polarizability. Furthermore, our calculations indicate that the Raman intensity decreases exponentially fast with the value of i. It follows that in practice only the LCM and possibly its first few overtones are within current detection capabilities.

Other low-frequency modes, such as in-plane bending, out-of-plane bending, and twisting, emerge from quantization of the other acoustic branches of infinite GNRs. They are also intrinsic signatures of the finite length of a GNR but they feature significantly smaller Raman intensity. These modes include: (i) In-plane bending vibrations emerge from the TA branches. They are Raman inactive for odd values of i ($\mathrm{B_{3u}}$ symmetry) and active for even values of i ($\mathrm{B_{2g}}$ symmetry). However, the bond-polarization model predicts that the maximum Raman intensity is small, for example it is only around 0.1% of the LCM for any overtone in a 5-AGNR of size $N = 8$; (ii) Twisting modes arise from the zone-folding of AGNR's ZA branch. These modes are either inactive (odd values of i – $\mathrm{A_u}$ symmetry) or active (even values of i – $\mathrm{B_{1g}}$ symmetry) with calculated maximum Raman intensity only around 0.5% of the LCM's for any overtone; and (iii) 1-ZA branch gives rise to out-of-plane bending modes which are either inactive (odd values of i – $\mathrm{B_{2u}}$ symmetry) or active (even values of i – $\mathrm{B_{3g}}$ symmetry). For the active out-of-plane bending modes, the Raman intensity is maximal for the first Raman active mode and is approximately 40% of the value of the LCM in the 5-AGNR of length $N = 8$, however this mode has a very low frequency ($9\,\mathrm{cm}^{-1}$), below the detection window of most spectrometers. In addition, Raman intensities for subsequent out-of-plane bending mode overtones decay exponentially and only reach around 12% of the LCM's intensity when averaged for all polarization directions (for a frequency of $81\,\mathrm{cm}^{-1}$, located close to the LCM at $84\,\mathrm{cm}^{-1}$). We emphasize that even though the numerical analysis presented here corresponds to the specific case of the 5-AGNR of length $N = 8$, the general qualitative conclusions remain valid for other finite GNR structures.

The simplicity of the zone-folding approach allows for obtaining a straightforward relationship of the LCM frequency as a function of length. Indeed, as the LA branch in GNRs is linear for a large portion of the Brillouin zone, we have:

$$\omega_i^{\mathrm{LCM}} = i\frac{\pi V}{L} \tag{2}$$

where $V = \sqrt{C/\rho}$ is the speed of sound, C is the elastic constant, and ρ is the material density. REBOII calculations indicate that $\pi V = 2954\,\text{Å}\,\mathrm{cm}^{-1}$. Equation 2, in practice valid for $i < N/2$, ignores chemical saturation at the end of the ribbons, but offers an accurate relationship allowing to experimentally determine the ribbon length from the measurement of the LCM frequency (and, possibly, its overtones). Finally, note that since V does not change with the GNR's width, the LCM modes only depend on the GNR's length.

SI Note 3 - DFT-calculated mode profiles

In addition to the mode frequencies and Raman intensities we also obtained the normal mode profiles from DFT- and REBOII-based calculations. Figure S5 shows the atomic displacement profiles from DFT for the LCM and its overtone, LCM3, for a finite size 10 units long 5-AGNR (10u-LCM *etc.*), as well as the normal mode profile for the RBLM. In addition, we plot the LCM and RBLM for the 8 unit, 6 unit, and 4 unit 5-AGNRs. Note, that for the latter two, the normal mode profile for the RBLM looses its purely transverse character as a result of the finite length of the GNR. We plot the profiles for both RBLM+ and RBLM- observed in the Raman spectra of samples with many short GNRs. We also show the LCM computed with the REBOII force-field for the three GNR widths of 10 units length (blue). We observe a lower frequency compared to the DFT-based calculations (5-AGNR) and experiments (7-/9-AGNR). For the other normal modes of the 7- and 9-AGNR we refer to our previous work.[3]

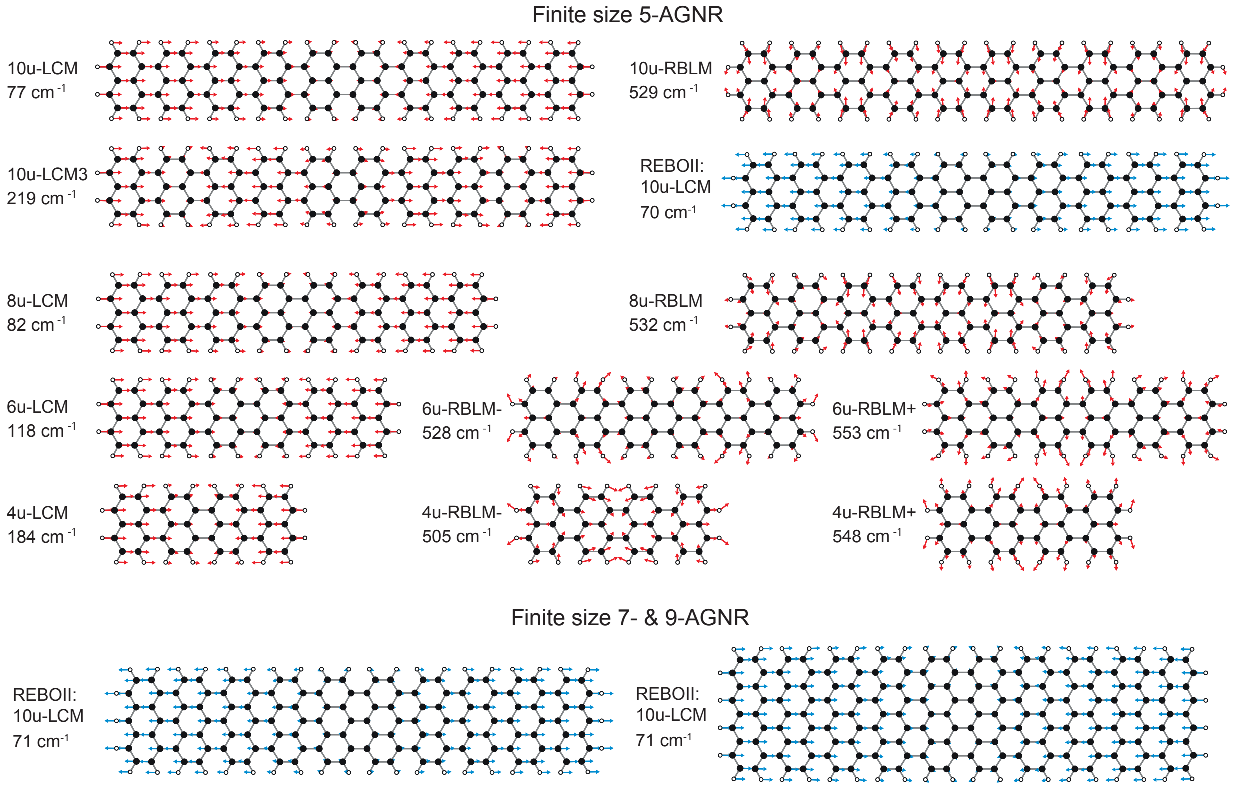

Figure S5: Normal mode profiles obtained from DFT/REBOII calculations (red/blue).

SI Note 4 - Additional Raman data

Measurement considerations

Acquisition of high quality Raman spectra relies on the optimization of several measurement parameters that have to be adjusted to the GNR under investigation. In general, we follow a mapping strategy and rely on Raman optimized (RO) device-type substrates (consisting of a layer structure of Si/SiO_2 and Au/Al_2O_3), as we have recently described elsewhere.[2] Here we highlight a few points of particular importance:

Excitation wavelength

We mainly used three wavelengths, 488 nm, 532 nm and 785 nm to characterize the samples (a further resonance Raman study combining measurements on multiple setups confirm these data and will be published elsewhere). For each type of GNR the excitation wavelength was chosen to give the strongest possible signal for the LCM.

The 5-AGNR has a small band gap in the range of ~ 0.5 eV, as deduced from STS data, and ~ 1.7 eV predicted by GW calculations before taking exciton binding into account[7]. Therefore, we predominantly used 785 nm (1.57 eV) for excitation, which is the lowest laser energy available in our setup and thus closest to resonance with the fundamental band gap. For the 7-AGNR, the 532 nm (2.33 eV) laser lies in between the reported $E_{1,1}$ and $E_{2,2}$ transitions and therefore gives a resonantly enhanced Raman signal.[1,3] Lastly, GW-calculations predict a band gap of 2.1 eV for the 9-AGNR, with strong exciton binding resulting in a lowest absorption peak expected at about 1 eV.[8,9] Even though the 785 nm laser is closer to the lowest energy transitions and results in the best signal for the RBLM, we observe the highest intensity of the LCM at an excitation wavelength of 488 nm. This points towards an electronic transition at a higher energy which is more strongly coupled to this particular vibrational mode.

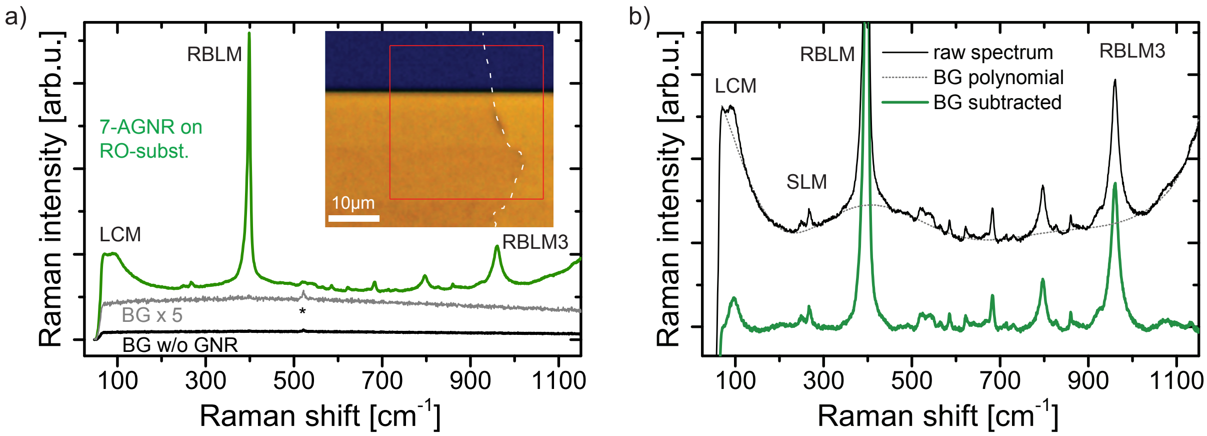

Figure S6: Mapping and background subtraction from raw data exemplified on 7-AGNRs. a) Raw spectra of 7-AGNRs grown on Au/Mica transferred to an RO-substrate. The inset shows an optical image of the sample area with the scan area indicated by a red square. The edge of the GNR film can be identified from the change in contrast on the Au-pad of the RO-substrate and is highlighted by a white dashed line. The GNR spectrum is obtained by averaging spectra from the bottom left side of the scan, the background spectrum by averaging in the GNR-free area of the same exact scan. $\lambda_{\text{exc}} = 532\,\text{nm}$, average over 100 (22) pixels for the GNR (BG) spectrum. Sample 7-1_T. **b)** Zoom in to the raw spectrum from a) before and after polynomial background subtraction. The polynomial is indicated by a dotted line.

Mapping, background subtraction and fitting

Throughout this work we employ a mapping strategy to acquire of high signal-to-noise spectra by averaging (up to several 1000 spectra), to make sure we report the average GNR properties and to exclude outliers produced by local contaminants.[2] This mapping approach also simplifies the identification of substrate effects. The inset in Figure S6 a) shows the outline (red line) of such a typical map on an RO device substrate. The edge of a GNR film is highlighted by a dashed white line. We average over a homogeneous part of such a Raman map (*e.g.* the bottom left quarter of that map) to get a high signal-to-noise spectrum. Such a map at the edge of the GNR film can further be used, to identify and exclude spurious effects from the substrate or setup.

Depending on the substrate and excitation wavelength, the raw spectra contain more or less background originating from both GNRs and the substrate.[1] To facilitate comparison between spectra obtained on different substrates and with different lasers (more or less resonant with the particular GNRs), we subtract a polynomial background fitted to the raw spectrum (masking peaks from the fit). Figure S6 shows an example of the procedure for a sample of 7-AGNRs transferred from Au/Mica.

Spectra for GNRs and background are obtained by averaging over the respective areas of the scan. The background obtained on the bare substrate after the Au-etching procedure is relatively low and completely featureless, except for a weak Raman peak of the Si-substrate (indicated by an asterisk) which originates from the residual transparency of the gold film. In particular, there is no (substrate- or setup-induced) intensity modulation in the background spectrum at low wavenumbers close to the onset of the filter. In contrast, the Raman spectrum shows several well defined peaks. Figure S6 b) shows the raw spectrum on a zoomed in scale, as well as the polynomial used for background subtraction and the resulting spectrum. Several settings for fitting the background polynomial were explored resulting in minor variability of absolute peak intensity and negligible influence on peak positions. Peak positions were obtained by fitting with a Lorentzian or Voigt profile.

Laser power

The GNRs are in contact with two fundamentally different substrates during Raman investigation, the Au substrate and a dielectric (SiO_2 or Al_2O_3). Similar to graphene, where it is well-known that the substrate strongly influences the optical properties, we also observe a much stronger Raman signal of the GNRs after transfer to a dielectric. Therefore, in analogy to Figures 4 and S12, we performed time-series measurements for each of the substrate-laser-wavelength combinations to choose the optimum integration-time and laser power while avoiding radiation-induced damage to the GNRs.

Reference measurements

In addition we performed reference measurements on both types of bare gold substrates, to exclude any non-trivial background contributing to the observed signal (see Figure S7 a)).

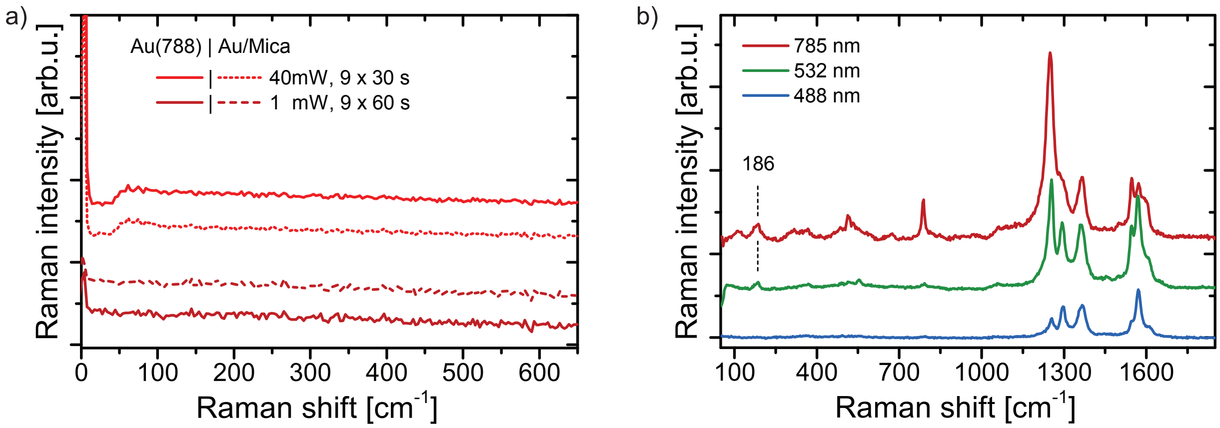

Figure S7: Reference measurements on bare gold and quaterrylene. a) Raman spectra of bare Au(788) and Au/Mica substrates in air for $\lambda_{\text{exc}} = 785\,\text{nm}$. Spectra are scaled to reveal the instrument noise level. No background subtraction was performed. **b)** Raman spectra on commercially available quaterrylene powder for three excitation wavelengths.

The settings cover the range of laser powers used for measurements of GNRs on gold and the integration time is longer than the maximum of 26 s used for Raman mapping. The spectra are scaled to reveal the noise floor of the instrument, up to which no Raman modes are observed.

As an independent reference measurement to compare with on-surface synthesized GNRs, in Figure S7 b) we show spectra obtained on commercially available quaterrylene (*Sigma Aldrich*). This substance corresponds to 4-units long 5-AGNRs and was measured in powder-form on a microscopy glass slide in air. The spectra for $\lambda_{\text{exc}} = 532/785\,\text{nm}$, which are closer to resonance of 5-AGNRs, show a peak at 186 cm^{-1}, the Raman shift at which the LCM is observed for on-surface synthesized ribbons and close to the value at which the 4u-LCM is expected based on DFT-calculations.

Raman spectra before & after transfer

Below we show spectra of 5-AGNRs both on growth substrate and after transfer. The fact that we can observe the LCM-187/125/98 after transfer clearly indicates the presence of short GNRs on the target substrate which can so far not be detected by other means. The

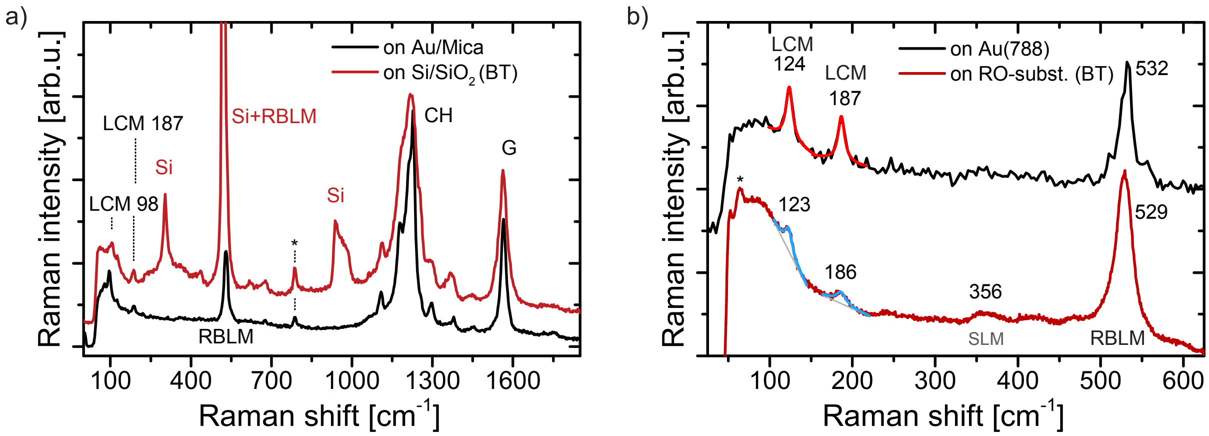

Figure S8: Spectra of 5-AGNRs on gold and after transfer to substrates. a) Full spectral range raw spectrum of 5-AGNRs on Au/Mica including background. This particular sample (5-2_Au) could not be imaged after transfer. A sample grown one day before with the same parameters but on Au(788) is shown after transfer to a standard Si-substrate. The most prominent peaks are labeled and peak positions are indicated. The peak labeled with an asterisk is discussed elsewhere.[2] $\lambda_{exc} = 785$ nm, Sample 5-7_T. **b)** Raman spectra of short 5-AGNRs grown on Au(788) before and after "bubbling transfer". The most prominent peaks are labeled and peak positions as obtained from Lorentzian fits are indicated. The intensity oscillations at and below ~ 75 cm^{-1} marked with an asterisk are artefacts from the 785 nm laser edge filter. $\lambda_{\mathrm{exc}} = 785$ nm, Samples 5-6_Au, 5-6_T.

slightly reduced intensity with respect to the RBLM fits to a lower transfer efficiency of short vs. long GNRs. For the LCM-98 we observe a slight up-shift after transfer to an oxide substrate, in line with our initial substrate-dependent findings on 9-AGNR as described in the main manuscript.

Spectra of 9-AGNRs on gold & on device-substrates and wavelength dependence

In Figure S9 a) we compare the Raman spectrum of 9-AGNRs obtained directly on Au(788) and after transfer to an RO-substrate. The much lower intensity of GNR Raman signal on gold and the background from the metallic Au(788) substrate prevent us from detecting or excluding the presence of the LCM on the growth substrate.

Figure S9 b) shows the spectrum of 9-AGNRs after BT onto an RO-substrate for three

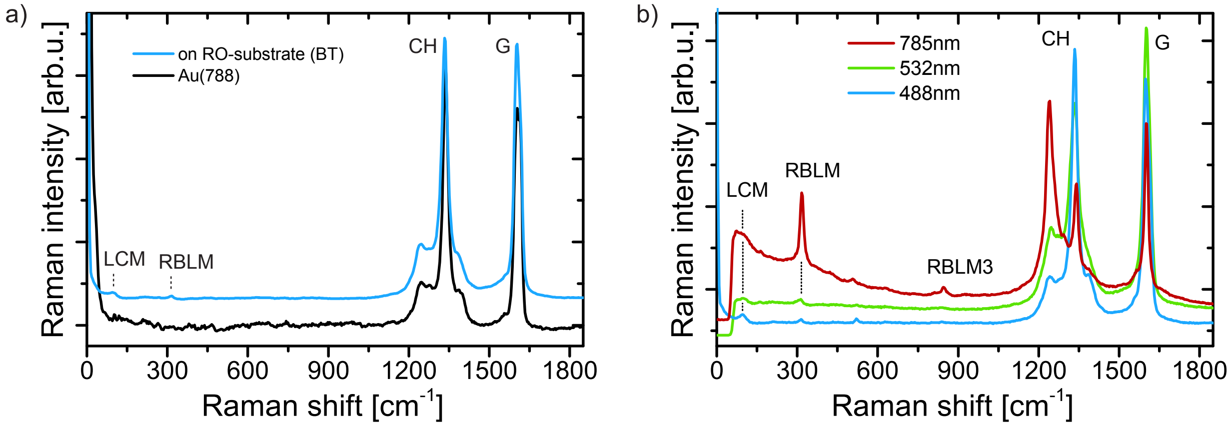

Figure S9: Raman spectra of 9-AGNRs. a) Comparison of a spectrum on Au(788), 9-3_Au, on an RO-substrate, Sample 9-1_T, scaled to a common G-peak intensity. $\lambda_{exc} = 488\,\text{nm}$. **b)** Raman spectra of 9-AGNRs after transfer to an RO-substrate for three excitation wavelengths. These spectra were acquired under ambient conditions and are arbitrarily scaled to highlight low-intensity features. Sample 9-4_T.

laser wavelengths. The LCM is most clearly observed at an excitation wavelength of $\lambda_{\text{exc}} = 488\,\text{nm}$ which corresponds to an energy significantly above the expected band gap of the 9-AGNR. For the other wavelengths, the LCM is less clear due to the onset of the edge filter in our setup. More extensive wavelength-dependent measurements are beyond the scope of this paper and are the subject of an ongoing study.

Polarization dependent measurements

We also performed polarization dependent measurements on aligned 7- and 9-AGNRs before (not shown) and after transfer. Unsurprisingly, these GNRs also show a strong dependence of Raman intensity on the Laser polarization direction θ. We fit each peak with a Lorentzian line shape and a linear background. The peak intensity follows a broadened $\cos^2(\theta)$ dependence as expected for a collection of dipoles (for an experimental configuration averaging over all angles in the detection path).[1] We use a simplified fitting model

$$I(\theta) = a \cdot \cos^2(\theta - \theta_0) + b \cdot \sin^2(\theta - \theta_0), \tag{3}$$

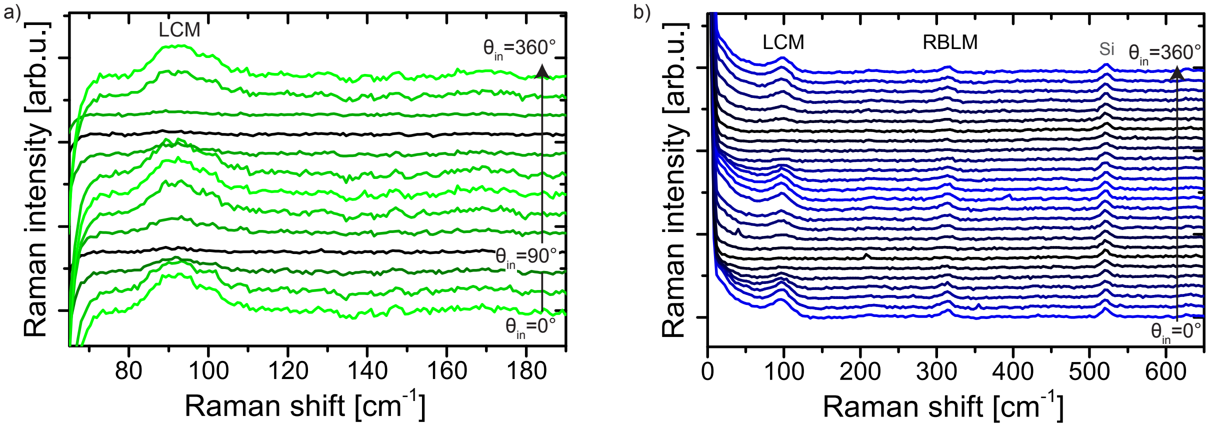

Figure S10: Polarization dependent spectra of the LCM for aligned 7- and 9-AGNRs. **a)** Polarization dependence of the LCM on a sample of aligned 7-AGNRs transferred to an RO-substrate. The polarization of the excitation was changed in steps of 30°. No polarizer was used in the detection path to maximize the overall signal. Large area average over 400 pixels. $\lambda_{exc} = 532\,\text{nm}$, Sample 7-2_T. **b)** Polarization dependence for aligned 9-AGNR on an RO-substrate. The polarization of the excitation was changed in steps of 15°. No polarizer was used in the detection path to maximize the overall signal. This measurement was performed under ambient conditions at an excitation wavelength of $\lambda_{\text{exc}} = 488\,\text{nm}$. Each spectrum is an average over 1430 pixels of a large area scan with reduced integration time, to avoid laser-induced damage to the ribbons. Sample 9-4_T.

where θ_0 is the misalignment between the Au(788)-terrace direction and the experimental axis defined as $\theta = 0$.

From this we extract the polarization anisotropy

$$P = \frac{I_\parallel - I_\perp}{I_\parallel + I_\perp} = \frac{a-b}{a+b}. \tag{4}$$

Figure S10 shows the polarization dependence of the low-energy region of the spectra for these two types of ribbons. 7-AGNRs were measured with resonant 532 nm excitation in vacuum to get the best signal-to-noise ratio. The LCM of 9-AGNRs is most clearly observed for an excitation wavelength of 488 nm, where our setup allows experiments at low Raman shifts. We measured consistent spectra of 9-AGNRs both in vacuum (not shown) and in air, which allows us to exclude any contribution from the window of the vacuum chamber.

We determine the polarization anisotropy for the different peaks. For the LCM, RBLM

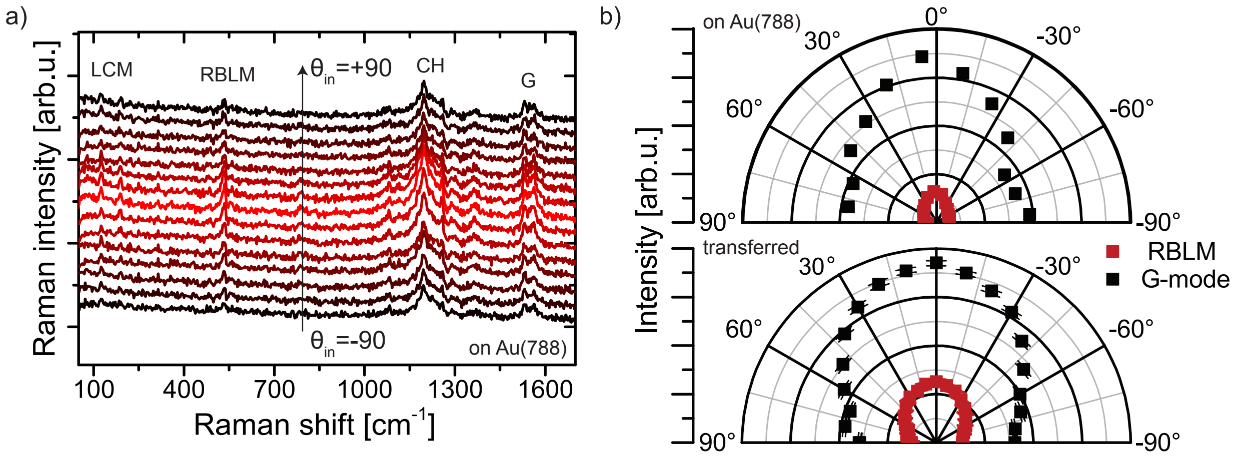

Figure S11: Polarization dependent spectra of short 5-AGNRs grown on Au(788) **a)** Raman spectra of short 5-AGNRs obtained directly on the Au(788) growth substrate. Analyzing polarizer $\parallel \theta_{in}$. $\lambda_{\mathrm{exc}} = 785\,\mathrm{nm}$. Sample 5-8_Au. **b)** Polar plots for RBLM and G-peak before and after GNR transfer (Sample 5-8_T). The polarization anisotropy is $\mathrm{P}_{\mathrm{RBLM,\,(G)}} = 0.4, (0.3)$ before and $\mathrm{P}_{\mathrm{RBLM,\,(G)}} = 0.4, (0.4)$ after transfer (no analyzing polarizer).

and G-peak (not shown) we find $\mathrm{P}_{\mathrm{LCM}} = 0.97$, $\mathrm{P}_{\mathrm{RBLM}} = 0.73$, $\mathrm{P}_{\mathrm{G}} = 0.72$.

We also investigated the polarization-dependence of 5-AGNR samples grown on Au(788) with a large number of short GNRs. As seen in the corresponding STM images in Figure S2, these ribbons are less well-aligned than GNRs grown with optimized parameters. This is reflected in the polarization anisotropy P, as shown in Figure S11.

SI Note 5 - Damage sensitivity, substrate interaction and length distribution

Radiation damaging of 9-AGNRs monitored *via* the LCM

Laser induced damage of nanomaterials is a well known problem in Raman spectroscopy. Above, we already discussed the mapping approach to mitigate this effect. On the other hand, the presence and shape of a Raman peak can be used as an indicator to assess the sample quality and investigate other sources of damage to the GNRs originating *e.g.* from sample fabrication.

In Figure 4 a) we show the evolution of the peak intensity of the LCM and other modes commonly looked at. The underlying spectra are shown in Figure S12 a) and are obtained by spatial averaging of subsequent scans of the same $3 \times 3\,\mu\text{m}^2$-area with 5 s integration time, each. Similarly, a power-dependent series (Figure S12 b)) with averaging over a $10 \times 10\,\mu\text{m}^2$-area was obtained. Integration time 1 s at 0.5 mW reduced to 0.1 s at 40 mW.

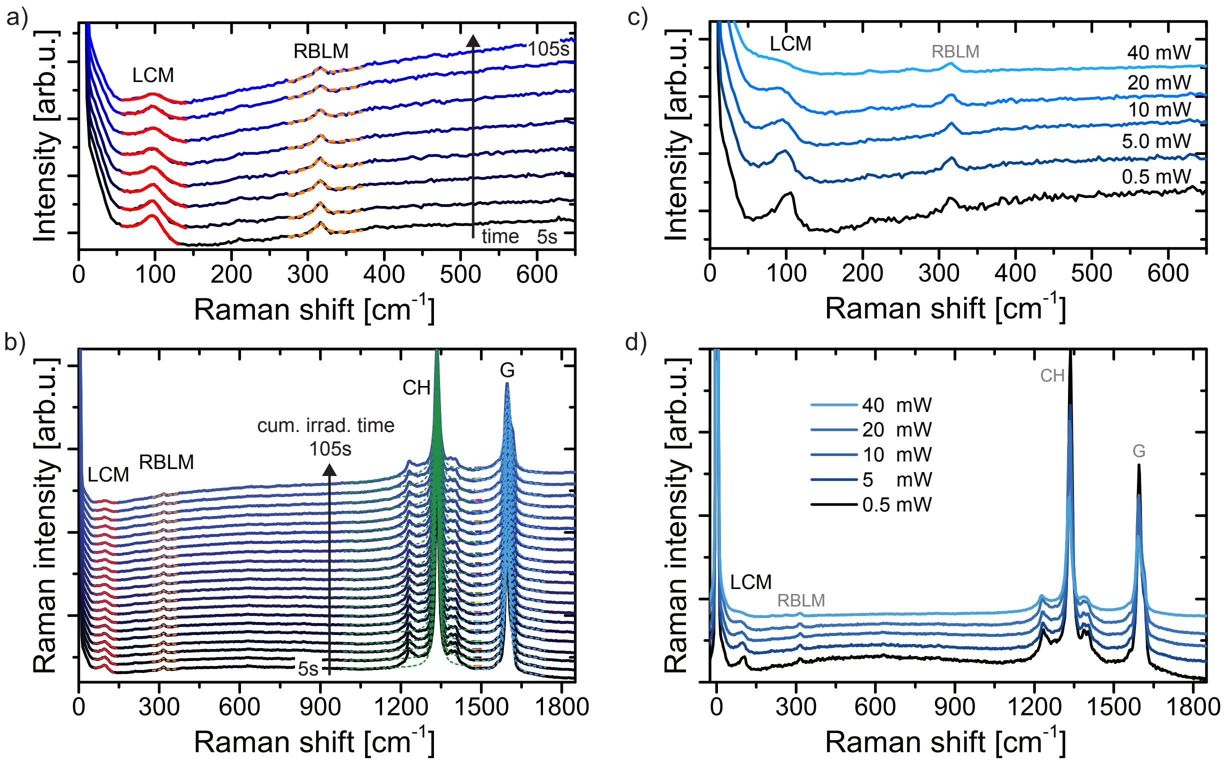

Figure S12: Radiation damaging of 9-AGNRs. **a)** Low-frequency Raman spectra over time, $t_{\text{int}} = 5\,\text{s}$, 15 s apart, $P = 5\,\text{mW}$. LCM and RBLM are fitted with a Lorentzian and linear background. **b)** Full spectral range of a) with the full series of spectra 5 s apart, including fits to CH- and G-peak. **c)** Power-dependent damaging. Spectra are scaled to a constant power-integration time product (0.5 mW x 1.1 s). **d)** Corresponding full-range spectra. All Sample 9-2_T and $\lambda_{\text{exc}} = 488\,\text{nm}$.

Substrate interaction

The substrate-dependent peak position of the LCM as shown in Figure 4 of the main manuscript was extracted by averaging GNR spectra acquired in a single map-scan covering both substrates, as shown in Figure S13. An intensity map of the G-peak / 2D-peak area of graphene (stronger, additional signal compared to GNR-only) can be used to identify pixels with/without graphene interlayer. Note, that the G-peak shift is within our experimental uncertainty and tends in the opposite direction of the shift observed for the LCM.

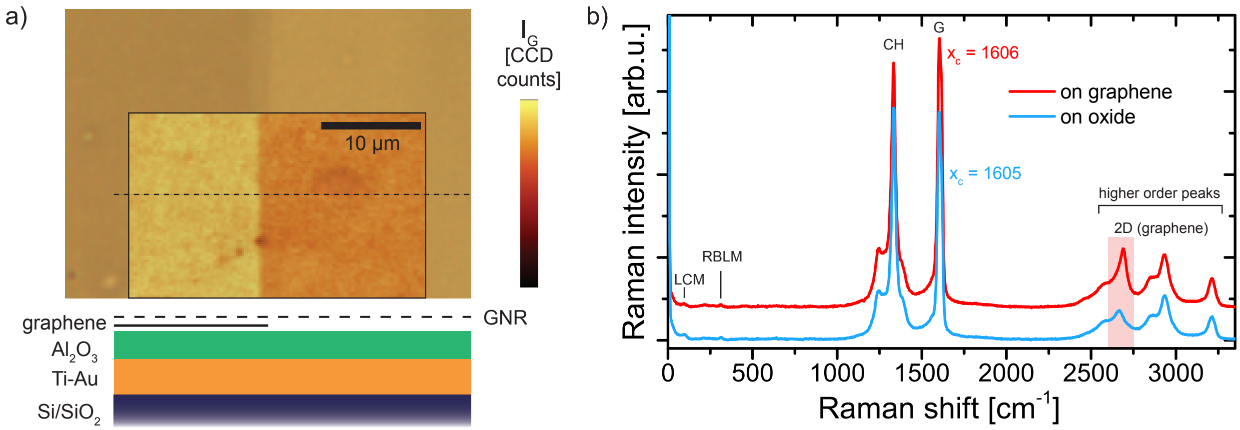

Figure S13: Mapping to probe the effect of different substrates on the LCM. a) Overlay of Raman map scan and optical microscope image showing GNRs on oxide (right) and on a graphene interlayer (left, darker contrast, higher G-peak intensity). Schematic of the sample layer structure. **b)** Full-range Raman spectrum extracted from a map scan as depicted in a and averaged over the respective substrate areas. G-peak position extracted from Lorentzian fit and graphene 2D-spectral region highlighted. P_{exc}=1 mW, λ_{exc} = 488 nm. Sample 9-1_T.

Summed REBOII Spectra

Typically, when experimental and calculated spectra are compared, the length distribution of ribbons is disregarded (as their aspect ratio is assumed to be very large). As we argue here, this is an oversimplification and taking into account the length distribution of ribbons on a sample is key, in order to be able to match calculations with experiments. As a first-order approximation, we can create simulated spectra for 5-AGNR films by taking the weighted sum of length-dependent REBOII-based spectra according to their percentage in the sample. The result of this for three different (artificial) length distributions is shown in Figure S14 a).

It can be seen, that this approach yields spectra with only minor variations for the RBLM, confirming that a length-independent treatment is valid for all samples with significant population of ribbons that are longer than 4 to 8 units, as only these shortest ribbons exhibit a splitting of the RBLM. In contrast, the simulated spectrum shows that the LCM-region is sensitive to variations in the dominant fraction of ribbons above 10 nm. A simulated spectrum assuming a length distribution concentrated on very short ribbons as observed for the

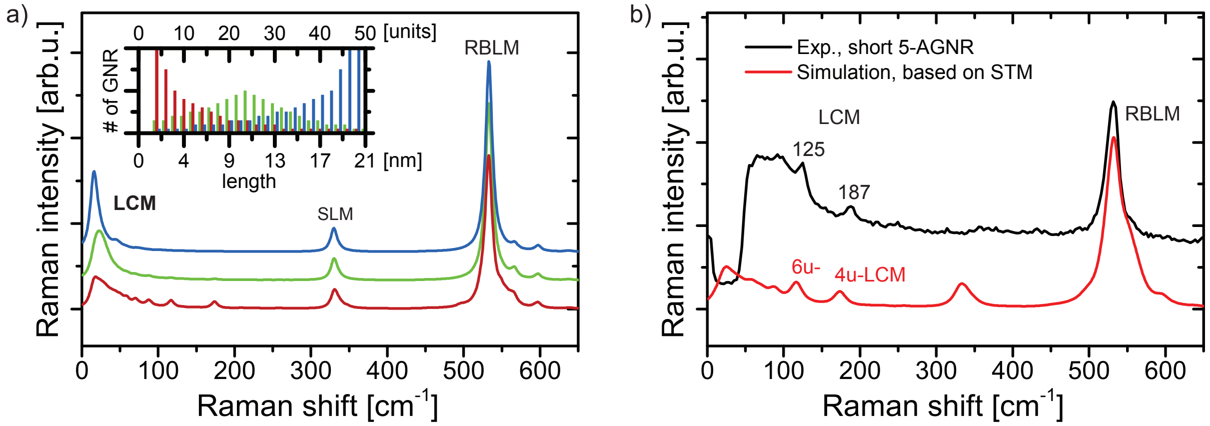

Figure S14: Simulated Raman spectra for 5-AGNR films. a) Simulated Raman spectra of 5-AGNR films obtained by summing REBOII-based spectra for 5-AGNRs of different length, weighted according to the three length-distributions shown in the inset (color coded short to long from bottom to top). b) Comparison of a simulated spectrum for a length distribution obtained from the STM of Sample 5-8_Au in Figure S2 b) to the corresponding experimental Raman spectrum spectrum after transfer (Sample 5-8_T).

5-AGNRs formed from partially dehydrogenated precursor molecules (see Figure S2 b) for corresponding STM image) is shown in panel b). It qualitatively matches the experimental data obtained on these ribbons even though aspects of substrate interaction as well as resonance Raman effects have not been taken into account. Improvements in these areas may in the future allow to extract the ribbon length distribution by fitting the weighting coefficients to experimental spectra.

References

1. Senkovskiy, B. V.; Pfeiffer, M.; Alavi, S. K.; Bliesener, A.; Zhu, J.; Michel, S.; Fedorov, A. V.; German, R.; Hertel, D.; Haberer, D.; Petaccia, L.; Fischer, F. R.; Meerholz, K.; van Loosdrecht, P. H. M.; Lindfors, K.; Grüneis, A. Making Graphene Nanoribbons Photoluminescent. *Nano Lett.* **2017**, *17*, 4029–4037.

2. Overbeck, J.; Borin Barin, G.; Daniels, C.; Perrin, M.; Liang, L.; Braun, O.; Darawish, R.; Burkhardt, B.; Dumslaff, T.; Wang, X.-Y.; Narita, A.; Müllen, K.; Meunier, V.; Fasel, R.; Calame, M.; Ruffieux, P. Optimized Substrates and Measurement Approaches for Raman Spectroscopy of Graphene Nanoribbons. *arXiv e-prints* **2019**, http://arxiv.org/abs/1907.01797 (accessed Sept. 19, 2019).

3. Borin Barin, G.; Fairbrother, A.; Rotach, L.; Bayle, M.; Paillet, M.; Liang, L.; Meunier, V.; Hauert, R.; Dumslaff, T.; Narita, A.; Müllen, K.; Sahabudeen, H.; Berger, R.; Feng, X.; Fasel, R.; Ruffieux, P. Surface-Synthesized Graphene Nanoribbons for Room Temperature Switching Devices: Substrate Transfer and *Ex Situ* Characterization. *ACS Appl. Nano Mater.* **2019**, *2*, 2184–2192.

4. Cai, J.; Ruffieux, P.; Jaafar, R.; Bieri, M.; Braun, T.; Blankenburg, S.; Muoth, M.; Seitsonen, A. P.; Saleh, M.; Feng, X.; Müllen, K.; Fasel, R. Atomically Precise Bottom-Up Fabrication of Graphene Nanoribbons. *Nature* **2010**, *466*, 470–473.

5. Di Giovannantonio, M.; Deniz, O.; Urgel, J. I.; Widmer, R.; Dienel, T.; Stolz, S.; Sánchez-Sánchez, C.; Muntwiler, M.; Dumslaff, T.; Berger, R.; Narita, A.; Feng, X.; Müllen, K.; Ruffieux, P.; Fasel, R. On-Surface Growth Dynamics of Graphene Nanoribbons: The Role of Halogen Functionalization. *ACS Nano* **2018**, *12*, 74–81.

6. Gillen, R.; Mohr, M.; Thomsen, C.; Maultzsch, J. Vibrational Properties of Graphene Nanoribbons by First-Principles Calculations. *Phys. Rev. B* **2009**, *80*, 155418.

7. Yang, L.; Park, C.-H.; Son, Y.-W.; Cohen, M. L.; Louie, S. G. Quasiparticle Energies and Band Gaps in Graphene Nanoribbons. *Phys. Rev. Lett.* **2007**, *99*, 186801.

8. Prezzi, D.; Varsano, D.; Ruini, A.; Marini, A.; Molinari, E. Optical Properties of Graphene Nanoribbons: The Role of Many-Body Effects. *Phys. Rev. B* **2008**, *77*, 041404.

9. Zhao, S.; Borin Barin, G.; Rondin, L.; Raynaud, C.; Fairbrother, A.; Dumslaff, T.; Campidelli, S.; Müllen, K.; Narita, A.; Voisin, C.; Ruffieux, P.; Fasel, R.; Lauret, J.-S. Optical Investigation of On-Surface Synthesized Armchair Graphene Nanoribbons. *Phys. Status Solidi B* **2017**, *254*, 1700223.